Calcified Tissue International (2023) 113:229–245
https://doi.org/10.1007/s00223-023-01098-9

ORIGINAL RESEARCH

The Contribution of Perilacunar Composition and Mechanical Properties to Whole-Bone Mechanical Outcomes in Streptozotocin-Induced Diabetes

Morgan W. Bolger[1] · Tara Tekkey[2] · David H. Kohn[1,3]

Received: 22 February 2023 / Accepted: 18 May 2023 / Published online: 1 June 2023

Abstract

Osteocytes are the most abundant cell type in bone and remodel their local perilacunar matrix in response to a variety of stimuli and diseases. How the perilacunar composition and mechanical properties are affected by type 1 diabetes (T1D), and the contribution of these local changes to the decline in whole-bone functional properties that occurs with diabetes remains unclear. 12–14 week old C57/BL6 male mice were administered a series of low-dose streptozotocin injections and sacrificed at baseline (BL), 3 (D3) and 7 weeks (D7) following confirmation of diabetes, along with age-matched controls (C3, C7). Femora were then subjected to a thorough morphological (μCT), mechanical (four-point bending, nanoindentation), and compositional (HPLC for collagen cross-links, Raman spectroscopy) analysis at the whole-bone and local (perilacunar and intracortical) levels. At the whole-bone level, D7 mice exhibited 10.7% lower ultimate load and 26.4% lower post-yield work relative to C7. These mechanical changes coincided with 52.2% higher levels of pentosidine at D7 compared to C7. At the local level, the creep distance increased, while modulus and hardness decreased in the perilacunar region relative to the intracortical for D7 mice, suggesting a spatial uncoupling in skeletal adaptation. D7 mice also exhibited increased matrix maturity in the 1660/1690 cm^{-1} ratio at both regions relative to C7. The perilacunar matrix maturity was predictive of post-yield work (46%), but perilacunar measures were not predictive of ultimate load, which was better explained by cortical area (26%). These results show that diabetes causes local perilacunar composition perturbations that affect whole-bone level mechanical properties, implicating osteocyte maintenance of its local matrix in the progression of diabetic skeletal fragility.

Keywords Biomechanics · Osteocyte · Perilacunar · Composition · Collagen · Diabetes

Introduction

In type 1 (T1D) and type 2 diabetes (T2D) there is a 6.94- and 1.38- times greater risk of hip fracture, respectively [1]. Individuals with T1D have a slightly lower bone mineral density (BMD), and those with T2D have a greater BMD than healthy age-matched controls. However, this increase in BMD with T2D is contradictory to the increase in fracture risk, and the small magnitude of the decrease in BMD with T1D is not enough to explain the 6.94-times greater risk of hip fracture [2]. For both type 1 and type 2 diabetes, increased glycation and decreased bone turnover are potential mechanisms of decreased bone strength and increased fragility [3–5]. Decreased bone turnover would increase overall tissue maturity, and hyperglycemia would glycate the collagen matrix forming advanced glycation end products (AGEs). Increased glycation is considered a mechanism of increased collagen matrix stiffness contributing to the decreased whole-bone post-yield properties and toughness that characterize the diabetic skeletal phenotype [2, 5–8].

While most analyses of diabetic skeletal fragility have focused on osteoblast or osteoclast behavior, recent work has identified osteocytes as more active contributors to skeletal phenotypes. The osteocyte is the most abundant cell type in bone and has been well established as a regulator of bone

✉ David H. Kohn
dhkohn@umich.edu

[1] Department of Biomedical Engineering, College of Engineering, University of Michigan, Ann Arbor, MI, USA

[2] Department of Chemistry, College of Literature, Science and the Arts, University of Michigan, Ann Arbor, MI, USA

[3] Department of Biologic and Materials Sciences, School of Dentistry, University of Michigan, 1011 N. University Ave., Ann Arbor, MI 48109, USA

formation and resorption [9]. Osteocytes also play a crucial role in maintaining and remodeling their local matrix and mineral environment [10]. In human bone, the osteocyte lacunar canalicular network (OLCN) has a large surface area of ~ 215 m^2, highlighting its importance in signaling and potential contribution to whole-bone mechanical properties [11]. Alterations in composition of the bone matrix surrounding the OLCN, specifically in perilacunar tissue, occur with lactation [12], exercise [13, 14], parathyroid hormone treatment [14], ovariectomy [15], glucocorticoid treatment [16], TGF-β signaling [17], MMP-13 signaling [18], chronic kidney disease [19], and vitamin D deficiency [20]. The primary compositional change to bone under diabetic conditions is a perturbed collagen matrix, specifically increased AGE formation, measured directly or spectroscopically [5, 21]. However, whether these compositional changes with diabetes occur uniformly throughout the bulk tissue or are site-specific (i.e. preferentially occurring in perilacunar tissue), or contribute to mechanical properties at the whole-bone level is unclear [22, 23].

With diabetes, osteocytes demonstrate reduced signaling under loading [24], and increased expression of sclerostin [25–27]. The only study examining perilacunar composition in a diabetic context showed a slight decrease in calcium content around the osteocyte [28]. The effect of diabetes on perilacunar mechanical properties is also unknown. A thorough characterization of perilacunar composition changes in diabetes, including changes in the collagen matrix, is needed to establish relationships between changes in perilacunar composition and mechanical properties, and how these local changes drive adaptation at the whole-bone level. The main questions of this study, investigated using a murine streptozotocin (STZ) model, were: (1) how are the local perilacunar composition and mechanical properties altered with diabetes, and (2) can local compositional and mechanical changes at the perilacunar zone contribute to changes at the whole-bone level.

Methods

Animal Study

All animal procedures and protocols were conducted with approval from the University of Michigan Institutional Animal Care and Use Committee (IACUC). Male C57BL/6 mice 8–10 weeks old were received for a baseline (BL) group, and 10–12 week old mice were received for the diabetic and control groups from Jackson Laboratory (Bar Harbor, ME). All mice were single housed with nesting enrichment for added sensory stimulation. After a 2-week acclimation period (at 12–14 weeks of age), mice were administered 5 daily intraperitoneal doses of streptozotocin (STZ, Sigma Aldrich S0130) at 50 mg/kg in a sodium citrate buffer while control mice received the sodium citrate buffer alone. Diabetic status was defined as blood glucose > 250 mg/dL and was confirmed after a 4-h fasting period with glucose measured via tail vein bleed (OneTouch Ultra2). Boosters of STZ at 50 mg/kg were administered weekly, if necessary, until mice became diabetic. Fasting blood glucose and body weight were measured weekly. Control mice were weight matched to diabetic groups at the time of initial STZ or buffer administration, and age matched. BL mice were sacrificed at 12–14 weeks of age. Mice were sacrificed after either 3 weeks (D3) or 7 weeks (D7) of diabetes, with age matched controls (C3, C7, respectively). Three and seven weeks were chosen based on literature suggesting at least 4-weeks are required for development of a diabetic skeletal phenotype with reductions in BMD and ultimate load [29]. At three weeks, we expected the diabetic skeletal phenotype to be developing, with early changes present, and an established phenotype by seven weeks. Mice were sacrificed via thoracotomy, cardiac puncture, and exsanguination under isoflurane. Whole blood was collected at endpoint for HbA1c measurements (A1CNow+, PTS Diagnostics, Whitestown, IN). All blood was stored at -80C until use. Femora and tibiae were immediately harvested and either processed for histology or stored at -80C in calcium-buffer saturated gauze [30]. Ultimately, this resulted in 20–24 mice per experimental group. Mice were randomly assigned to one of two subsets where for subset 1, left femora (n = 10–12/group) were imaged by microCT then subjected to four-point bend, right femora (n = 5–6/group) were tested by nanoindentation then Raman spectroscopy and for subset 2, left femora were subject to immunohistochemistry (n = 7/group, excluding BL), and right femora were used for collagen cross-link quantification by HPLC (n = 10–12/group).

MicroCT—2D & 3D Bone Morphology

Left femora (n = 10–12/group) were scanned by μCT (μCT100 Scanco Medical, Bassersdorf, Switzerland), with the following settings: 12 μm voxel size, 70kVP, 114 μA, 0.5 mm AL filter, and 500 ms integration time. All density and 3D analysis of cortical (Ct) were conducted on the Scanco evaluation software to calculate total volume (Ct.TV), bone volume (Ct.BV), bone volume fraction (Ct.BV/TV), bone mineral density (Ct.BMD) and tissue mineral density (Ct.TMD). 3D cortical analysis and density measurements were taken over 40 slices (480 μm) centered on the middle of the diaphysis, at a 28% global threshold (280 on a grayscale of 0–1000) using the manufacturer's software. 3D trabecular (Tb) analysis was carried out just proximal to the growth plate, over 40 slices (480 μm), excluding the surrounding cortical bone, with a 18% global threshold (180 on a grayscale of 0–1000) consistent with prior studies

[31]. Using the manufacturer's software, trabecular bone volume fraction total volume (Tb.TV), bone volume (Tb.BV), bone volume fraction (Tb.BV/TV), bone mineral density (Tb.BMD), tissue mineral density (Tb.TMD), thickness (Tb.Th), number (Tb.N), separation (Tb.Sp), connectivity density, and structural model index were all calculated. 2D analysis at the mid-shaft of the cortex was conducted on exported DICOM files with the BoneJ and MomentMacro (Momentmacro.J; www.hopkinsmedicine.org/fae/mmacro.html) plugins on ImageJ to measure total cross-sectional area (Tt.Ar), cortical area (Ct.Ar), marrow area (Ma.Ar), perimeter (Ct.Pm), moments of inertia about the anterior–posterior (I_{AP}) and medial–lateral axes (I_{ML}), distance from centroid to posterior surface and mean cortical thickness [32]. All ASBMR standards were followed [33].

Four-Point Bending

After μCT scanning, the femora were returned to -80C until mechanical testing, and prior to mechanical testing they were allowed to come to room temperature and subjected to four-point bending on an eXpert 450 Universal Testing Machine (Admet, Norwood, MA) with a 1500 ASK-100 load cell (Interface, Scottsdale, AZ). Bones were hydrated with calcium buffered PBS, and monotonically tested to failure after a preload of 0.5N, at a 0.01 mm/sec rate, and the anterior surface in tension. The equipment had an upper loading span of 3.00 mm and support span of 9.15 mm. The 0.2% offset method was used to calculate the yield point, and tissue-level properties were estimated using beam theory based on the mid-diaphyseal cross-section geometry and calculated using custom Matlab (Mathworks, Natick, MA) scripts, as described [34]. A surrogate measure of toughness, work-of-fracture was also calculated as work normalized to twice the cross-sectional area [35, 36].

Collagen Cross-link Quantification

Collagen cross-link and AGE quantification followed established protocols [13, 37, 38]. Right femora (n = 10–12/group) had the distal and proximal epiphyses removed, the bone marrow flushed with PBS, and the mineralized weight recorded. Bones were demineralized using 0.5 M ethylenediaminetetraacetic acid (Sigma Aldrich, E5134), pH = 8, at 4 °C under constant agitation for 4 days. Bones were then washed repeatedly with distilled water, demineralized weight recorded, and then diced and kept in PBS while subjected to sodium borohydride reduction for 1 h at room temperature. After repeated washing with distilled water, samples were kept in TAPSO buffer (Sigma Aldrich, T9269) and denatured at 110 °C for 35 min. After allowing samples to equilibrate to temperature in a 37 °C incubator, samples were digested with TPCK-treated trypsin (Thermo Scientific, PI20233) under constant gentle agitation for 48 h. Samples were then defatted using 3:1 (v:v) choloroform:methanol, and a portion of the tryptic digest was set aside for pyrrole cross-link quantification [39]. The remaining tryptic digest was subject to acid hydrolysis with a 1:1 addition of 12N hydrochloric acid and hydrolyzed for 24 h at 110 °C. A small amount of hydrolysate was diluted and used for colorimetric quantification of hydroxyproline [40]. The hydrolysate was then spiked with an acetylated pyridinoline as an internal standard (INT-STD., Quidel, San Diego, CA, Cat. #8006), cleaned by using an SPE column (Bond Elut-Cellulose, 12102095, Agilent, Santa Clara, CA), eluted, lyophilized and reconstituted in the initial gradient starting conditions for HPLC quantification.

Quantification of the divalent immature enzymatic cross-links: dihydroxy-lysinonor-leucine (DHLNL), hydroxy-lysino-norleucine (HLNL), mature tri-valent enzymatic cross-links: pyridinoline (PYD), deoxypyridinoline (DPD), and the AGE pentosidine (PEN) was conducted on a Waters 1525 Binary Pump (Waters Corp., Milford, MA, USA) with an Atlantis T3 column (Waters Corp., 186003728) and guard column at 30 °C. Solvent A: 0.12% (v) heptafluorobutyric acid (Sigma, 52411); Solvent B: 50/50 (v/v) water/acetonitrile and all solvents were HPLC grade. All cross-link species and internal standard (INT-STD) were quantified from a single 50 μL injection with flow at 1 mL/min and the following gradient: 0 to 40 min (91%A:9%B to 81%A:19%B), 40 to 60 min (81%A:19%B to 70%A:30%B), held from 60 to 65 min, then re-equilibrated to initial conditions between sample runs. A post-column reaction of o-pthaldiadehyde solution was added via. a high pressure syringe pump (Nexus 5000, Chemyx, Stafford, TX, USA) at a flow rate of 0.25 mL/min [37]. After detection of immature cross-links, the pump was turned off and the baseline recovered prior to detection of PYD, DPD, INT-STD, and PEN. See Supp. Figure 3D for representative chromatograms. Standards of PYD, DPD (Quidel, San Diego, CA), DHLNL (Santa Cruz Biotech, sc-20759C), and PEN (Cayman Chemical, 10010254) were purchased from commercial vendors. As no commercial source of HLNL was available, DHLNL was used as the standard curve for HLNL as well. All cross-link species were normalized to collagen content determined by the hydroxyproline content. Concentrations of individual cross-links are reported, and ratios are reported in the supplementary material (Supplemental Table 3).

Nanoindentation

Right fresh-frozen femora (n = 5–6 per group) were thawed and embedded in poly methyl methacrylate (Koldmount, SPI Supplies) and allowed to cure at room temperature overnight. Embedded bones were then transversely cut at the midshaft with a low-speed circular diamond saw (South Bay Technology, Model 650, CA). The proximal portion

of the block was polished with a series of coarse to fine grit sandpaper increasing from 2400 to 3000 to 4000, then polished with a 0.25 µm diamond suspension, and subjected to a 5 min sonic bath in calcium buffered PBS [30]. Tissue blocks were wrapped in calcium buffered PBS gauze and stored at −20 °C until further testing.

Local mechanical properties were assessed by nanoindentation (n = 5–6 indentations/location; 12–14 indents/bone) with indents taken at two locations in the anterior quadrant; 1) perilacunar: less than 5 µm from a lacunae wall, and 2) intracortical: greater than 20 µm from any visible lacunae (Supp. Figure 3A). Indentation was conducted on a 950 TI TriboIndenter (Hysitron, Minneapolis, MN, USA). Lacunae were visualized and nanoindentation locations were assigned using the 950 TI TriboIndenter, outfitted with a 20X objective lens, with up to 11X digital magnification. Indentation locations were confirmed before and after the loading scheme applied. The loading scheme was adapted from previous methodology [41]. A Berkovich tip was loaded at 2mN/s for 5 s, then held at 10mN for 60 s to examine creep behavior, and unloaded at 2mN/s. Indentation was conducted in a humid state with calcium buffered PBS. Young's modulus and hardness were extracted from the unloading segment of the load–displacement curve with the Oliver-Pharr method [42]. Plastic and elastic work were calculated from the respective integrated areas, and plastic index calculated as the plastic work normalized to the total work (elastic + plastic work). The creep behavior was extracted from the first 30 s of the holding period with custom a Matlab code (adapted from [43]) to fit the experimental data to the Burgers model [41], which strongly fit the data ($R^2_{adj} > 0.999$ for all individual indents; Supp. Figure 3B). The distance the tip moved into the tissue over the constant load was defined as the creep distance. The Burgers model consists of a spring and damper in series with a parallel pair of a spring and damper (Supp. Figure 3C). This model yields values for the instantaneous modulus (E_1) and instantaneous viscosity (η_1) as well as the long-term modulus (E_2) and parallel viscosity (η_2) to yield the viscoelastic time constant (τ).

Raman Spectroscopy

After nanoindentation, Raman spectroscopy was conducted on the same (n = 5–6 per group) embedded tissue blocks to measure the local composition, using the same criteria for perilacunar and intracortical regions as with nanoindentation. As an additional requirement, no Raman measurements were taken over the visible indented locations to prevent any perturbations caused by the indent from influencing the spectra. Raman spectroscopy acquisition was adapted from established methods [14, 37, 44]. Briefly, using 20X/0.75 NA objective, a 10 nm laser spot was placed at the aforementioned regions (5–6 scans/location, 10–12/sample), and after a 4-min photobleach to minimize background fluorescence, two spectra were acquired over a 7 min period (2 × 3.5 min). All spectra were calibrated, processed and polymer background subtracted in Matlab (Mathworks, Natick, MA) with custom scripts described elsewhere [44]. Spectra were then manually baselined and peak-fitted in GRAMS/AI (Thermo Fisher, Madison, WI) using published protocols [44]. Specific bands of interest were the phosphate band at ~ 959 cm^{-1}, carbonate at ~ 1070 cm^{-1}, proline at ~ 853 cm^{-1}, hydroxyproline at ~ 876 cm^{-1}. Bands of interest from the amide I region were ~ 1660 cm^{-1}, and ~ 1690 cm^{-1} (ratios based on other amide I bands ~ 1683 cm^{-1} and ~ 1631 cm^{-1} are included in Supp. Table 5). Bands of interest from the amide III region were ~ 1243 cm^{-1}, and ~ 1268 cm^{-1}. Calculated measurements presented include the proline/hydroxyproline ratio (876/853 cm^{-1}), crystallinity (1/FWHM 960 cm^{-1}), mineral-to-matrix (MMR, 960/(876 + 853) cm^{-1}), carbonate/phosphate (1070/959 cm^{-1}), amide I (1660/1690 cm^{-1}) and amide III (1243/1268 cm^{-1}) ratios. Both height and area ratios were calculated. All Raman measures presented in the body of the text are based on peak height, those based on both height and area are provided in Supp. Table 5.

LOX & RAGE Immunofluorescent Staining

Left femora were immediately placed in 0.5 M ethylenediaminetetraacetic acid (Sigma Aldrich, E5134), pH = 7.6, at 4C for decalcification lasting approximately 2 weeks. After three 60-min washes in PBS at 4 °C, bones were transferred to 70% ethanol and then embedded in paraffin and stored at room temperature until sectioning. 5 µm longitudinal sections from each block were obtained (n = 7 bones per group). Samples were stained in triplicate with a control lacking primary antibody. Sections were co-stained for LOX (Abcam; ab174316, 1:100) and RAGE (R&D Systems; af1179, 1:15) with secondary anti-rabbit Alexa Fluor 488 (Abcam; ab150073, 1:200), and anti-goat Alexa Fluor 594 (Abcam; ab150132, 1:800) antibodies according to manufacturer (Abcam) protocols. Samples were then mounted in Fluoromount-G with DAPI (SouternBiotech, OB100-01) and sealed. Sections were imaged on a Leica DMi8 Thunder imager microscope (Leica Systems, Wetzlar, Germany), with a 20X objective, 0.8 numerical aperture, and acquired on a Leica DFC9000 camera at 2048 × 2048. Each image was then subjected to instant computational clearing accounting for the refractive index of the Fluoromount-G being ~ 1.4.

3–4 images per slice and 3 slices per bone were analyzed in ImageJ [32]. Images were cropped to an intracortical region of interest, excluding the endosteal and periosteal surface and any vasculature. The DAPI channel was used to calculate osteocyte number and density, and to create a mask over which the LOX and RAGE signal was quantified within the DAPI signal using the Coloc2 plugin. All intensity-based

measurements were normalized to the respective mean of the C3 group. Due to experimental limitations, BL bones were not available for immunofluorescent staining.

Correlation Analysis and Statistics

All statistical analyses were carried out in Matlab 2021a (Mathworks, Natick, MA). To test for group differences—for all experiments besides nanoindentation and Raman spectroscopy—between C3, D3, C7, and D7, a two-way ANOVA with Tukey's post-hoc test was conducted, and significant ($p < 0.05$) factor effects for diabetes (D), time (T) and their interaction (DxT) was noted. A one-way ANOVA with Fisher's least significant difference post-hoc was conducted to compare BL to C3, D3, C7 and D7. For nanoindentation and Raman spectroscopy, two-way ANOVA with Tukey's post-hoc test was carried out for C3, D3 and separately for C7, D7 with control/diabetic and intracortical/perilacunar as the two factors. Two-way ANOVAs were also carried out for BL compared to all groups with group and intracortical/perilacunar as the two factors. Significant factor effects for diabetic status (D), location (L) and diabetic status-location interaction (DxL) are indicated. Significance for all tests was defined as $p < 0.05$, with trends of $0.05 < p < 0.10$ noted in the figures with their corresponding p-value. Data in Figs. 1, 2, 3 are presented as mean overlaid with individual data points. Data in Figs. 4, 5 are presented as mean ± standard deviation. Data in Table 1 is presented as mean (standard deviation) for each group. To test whether local composition and mechanical measures could explain whole-bone behavior, a correlation and regression analysis was conducted. Table 2 presents significant Pearson correlation coefficients of interest. From this initial screen, linear regressions were conducted (Fig. 6).

Results

Diabetes Increased Fasting Blood Glucose, HbA1c and Prevented Weight Gain

Administration of the low dose streptozotocin induced a diabetic state. Animals in diabetic states for 3 (D3) and 7 weeks (D7) had significantly higher fasting blood glucose (Fig. 1A) than baseline mice ($p < 0.001$ for both), 3 week control (C3, $p < 0.001$ for both) and 7 week control (C7, $p < 0.001$ for both). D7 mice also exhibited significantly greater fasting blood glucose than D3 ($p < 0.001$) and factor effects for diabetes (D, $p < 0.001$), time (T, $p = 0.002$) and the interaction (DxT, $p = 0.001$) were all significant. All differences detected for fasting blood glucose were also detected for HbA1c. D3 and D7 mice exhibited increased HbA1c (Fig. 1B) compared to BL ($p < 0.001$ for both), C3 ($p < 0.001$ for both) and C7 ($p < 0.001$ for both). D7 mice also had a significantly higher HbA1c than D3 mice ($p < 0.001$ for both) and factor effects of diabetes, time and DxT ($p < 0.001$ for all) were significant. No difference in fasting blood glucose or HbA1c was detected between BL, C3, and C7 mice. The average weight of the C3 and C7 groups was significantly higher than BL ($p < 0.001$ for both), D3 ($p < 0.001$ for both) and D7 ($p < 0.001$ for both) with no difference between C3 and C7 mice (Fig. 1C). Significant factor effects with body weight

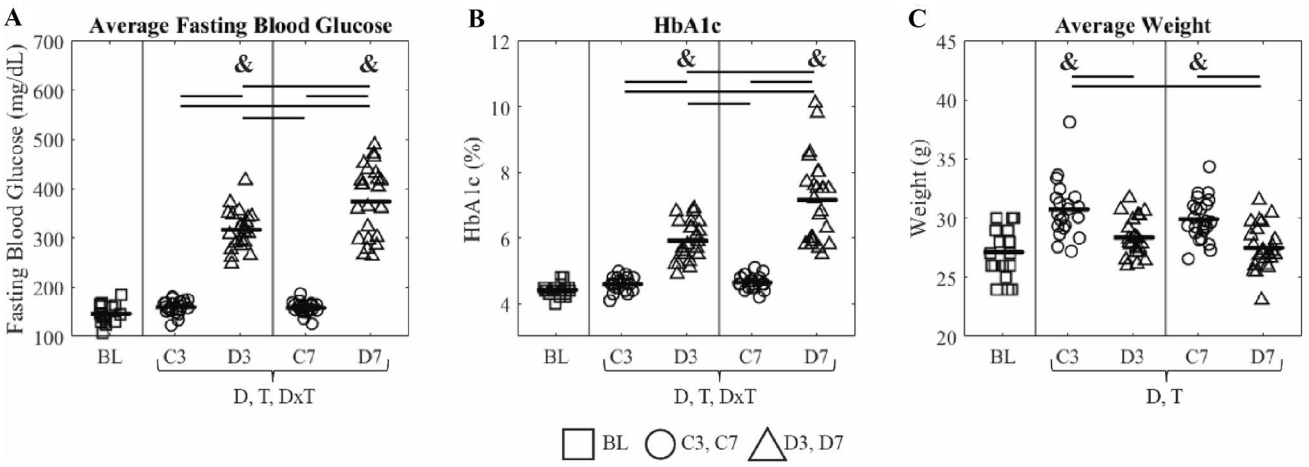

Fig. 1 Animal Diabetic Status and Body Weight. **A** Average fasting blood glucose, **B** percent of glycated hemoglobin (HbA1c), and **C** average body weight for baseline (BL), 3-week control (C3), 3-week diabetic (D3), 7-week control (C7) and 7-week diabetic (D7). Data are presented as means with individual data points for each group. Two-way ANOVAs were carried out for C3, D3, C7, and D7 and significance ($p < 0.05$) between groups after Tukey's post-hoc tests is indicated by horizontal bars. Significant factor effects ($p < 0.05$) for diabetic status (D), time (T) and diabetic status-time interaction (DxT) are indicated below the x-axis. One-way ANOVAs with least-squares difference post-hoc tests were carried out to detect significant differences relative to BL and are indicated by & ($p < 0.05$)

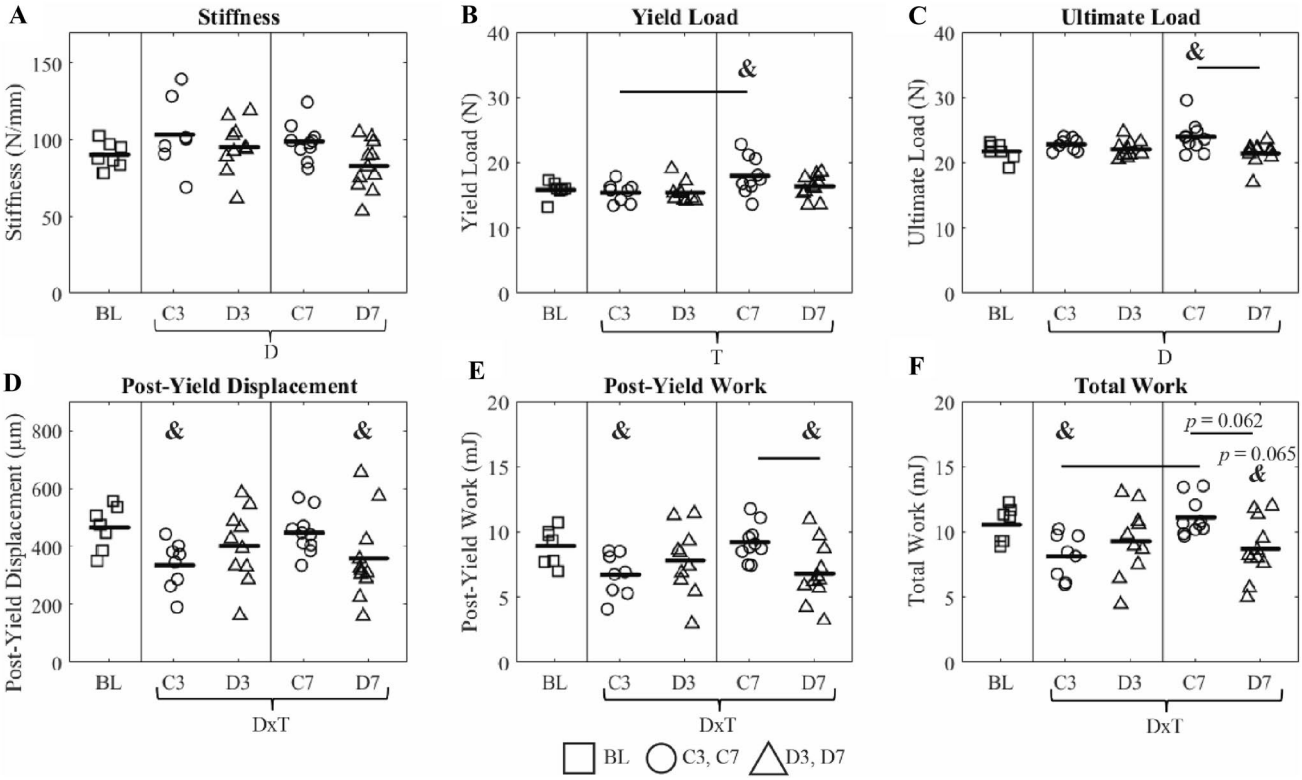

Fig. 2 Whole-bone mechanical properties. **A** stiffness, **B** yield load, **C** ultimate load, **D** post-yield displacement, **E** post-yield work, **F** total work for baseline (BL), 3-week control (C3), 3-week diabetic (D3), 7-week control (C7) and 7-week diabetic (D7) mice. Data are presented as means with individual data points for each group. Two-way ANOVAs were carried out for C3, D3, C7, and D7 and significance ($p < 0.05$) between groups after Tukey's post-hoc tests is indicated by horizontal bars. Significant factor effects ($p < 0.05$) for diabetic status (D), time (T) and diabetic status-time interaction (DxT) are indicated below the x-axis. One-way ANOVAs with least-squares difference post-hoc tests were carried out to detect significant differences relative to BL and are indicated by & ($p < 0.05$)

were detected for diabetes ($p < 0.001$) and time ($p = 0.041$). There was no significant difference in body weight between BL, D3 and D7 mice.

The 7-Week Diabetic Group Exhibited Decreased Ultimate Load, Post-yield Work and Increased Pentosidine Relative to Age-Matched Controls

Both D7 and D3 mice had a significantly lower cortical bone volume fraction (Ct.BV/TV) than BL (Table 1, $p = 0.045$, $p = 0.004$) with a significant diabetes factor effect ($p = 0.032$). No difference in Ct.BV/TV was detected between BL, C3, and C7 mice. Additionally, Ct.BMD trended lower for D7 mice relative to C7 ($p = 0.087$). All groups exhibited higher Ct.TMD relative to BL (C3, $p = 0.003$; D3, $p < 0.001$; C7, $p < 0.001$; D7, $p < 0.001$). There was no difference in total area between groups, but a diabetes factor effect ($p = 0.017$) was detected for cortical area. Only C3 mice exhibited greater marrow area ($p = 0.046$) and perimeter ($p = 0.036$) relative to BL. The mean cortical thickness trended lower in D7 mice relative to C7 mice ($p = 0.074$), and cortical thickness in both D3 and D7 mice was significantly lower compared to BL ($p = 0.027$, $p = 0.002$), with a significant diabetes factor effect ($p = 0.004$). No significant difference was detected between any group for the moment of inertia about the medial–lateral or anterior–posterior axes. Few differences in 3D trabecular parameters were detected with diabetes, and the most significant effects were relative to BL (Supp. Table 1).

At the whole-bone level, D7 mice exhibited significantly lower ultimate load relative to C7 mice ($p = 0.007$), and C7 mice exhibited significantly greater ultimate load compared to BL ($p = 0.008$), with a significant factor effect of diabetes ($p = 0.005$, Fig. 2C). D7 mice also exhibited significantly lower post-yield work relative to C7 ($p = 0.0497$) and BL ($p = 0.032$). Post-yield work in C3 mice was significantly lower relative to BL ($p = 0.038$), and a significant DxT factor effect was detected ($p = 0.012$, Fig. 2E). A significant factor effect of diabetes was detected for stiffness ($p = 0.033$, Fig. 2A). C7 mice exhibited a significantly greater yield load (Fig. 2B) relative BL ($p = 0.029$), with a significant factor effect for time ($p = 0.010$). C3 and D7 mice exhibited significantly lower post-yield displacement (Fig. 2D) relative to BL ($p = 0.026$, $p = 0.048$) with a significant

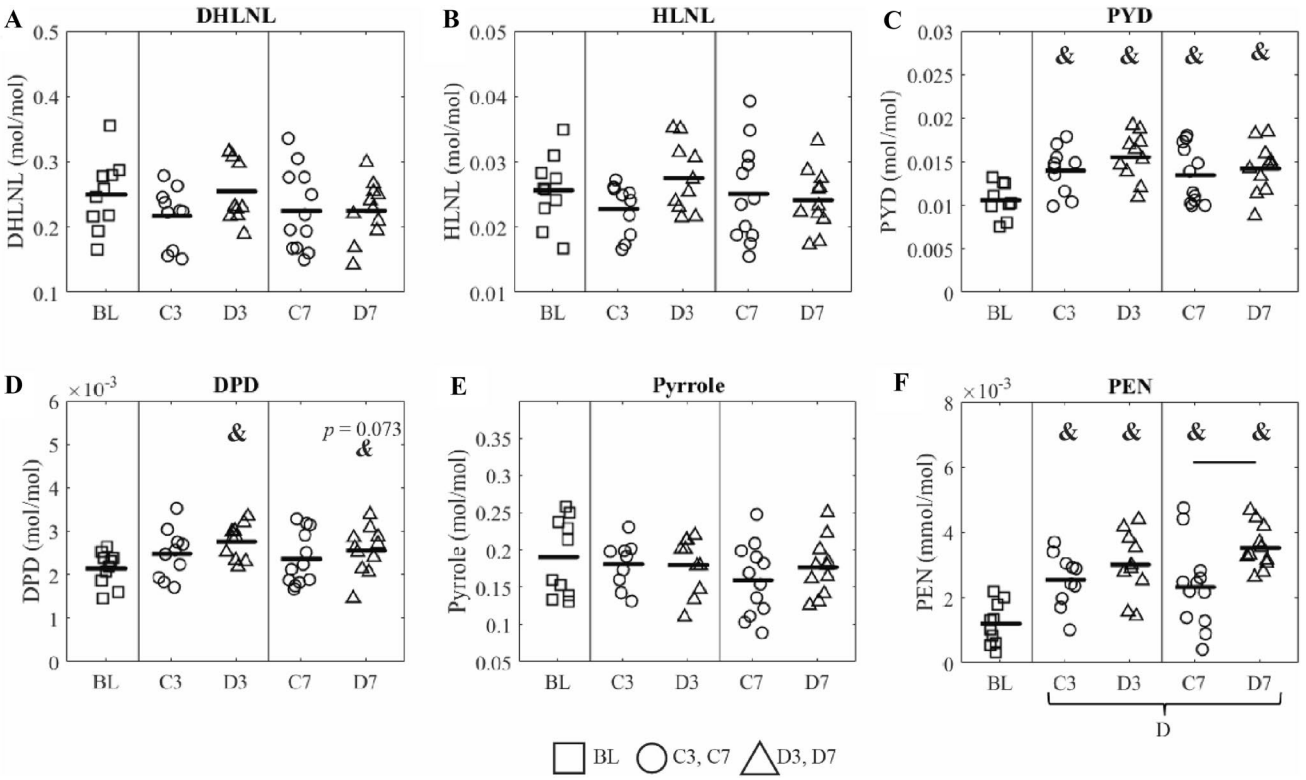

Fig. 3 Collagen cross-links and the advanced glycation product pentosidine. Divalent immature enzymatic cross-links: **A** dihydroxylysinonor-leucine (DHLNL), **B** hydroxy-lysino-norleucine (HLNL), mature tri-valent enzymatic cross-links: **C** pyridinoline (PYD), **D** deoxypyridinoline (DPD), **E** pyrroles, **F** advanced glycation end-product pentosidine (PEN) for baseline (BL), 3-week control (C3), 3-week diabetic (D3), 7-week control (C7) and 7-week diabetic (D7) mice. Data are presented as means with individual data points for each group. Two-way ANOVAs were carried out for C3, D3, C7, and D7 and significance ($p < 0.05$) between groups after Tukey's post-hoc tests is indicated by horizontal bars. Significant factor effects ($p < 0.05$) for diabetic status (D), time (T) and diabetic status-time interaction (DxT) are indicated below the x-axis. One-way ANOVAs with least-squares difference post-hoc tests were carried out to detect significant differences relative to BL and are indicated by & ($p < 0.05$)

diabetes x time interaction ($p = 0.041$). C3 mice demonstrated lower total work (Fig. 2F) relative to BL ($p = 0.026$) and C7 ($p = 0.027$) with a significant interaction DxT effect observed ($p = 0.013$).

Differences in estimated tissue-level properties between groups were more subtle. Similar to yield load, yield stress (Supp. Figure 1B) had a significant factor of time ($p = 0.008$). The ultimate stress (Supp. Figure 1C) trended lower for the D7 group relative to C7 ($p = 0.076$) with a significant DxT interaction ($p = 0.041$). The post yield strain (Supp. Figure 1D) was significantly lower in C3 relative to BL ($p = 0.0496$), and trending lower in D7 ($p = 0.079$) relative to BL, with a significant DxT interaction ($p = 0.043$). These same relationships were observed for post-yield toughness (Supp. Figure 1E), with values significantly lower in C3 mice relative to BL ($p = 0.043$), trending lower in D7 mice relative to BL ($p = 0.086$) and significant DxT interaction ($p = 0.018$). The total toughness (Supp. Figure 1F) was significantly lower in C3 mice relative to BL mice ($p = 0.030$), with a significant interaction DxT as well ($p = 0.019$). Consistent with total toughness, the work of fracture (Supp. Figure 1G) was significantly lower in C3 relative to BL mice ($p = 0.032$), with a significant DxT interaction ($p = 0.038$). No significant difference between groups was detected for modulus (Supp. Figure 1A). All mechanical outcomes are provided in the supplemental as well (Supp. Table 2).

The concentration of PEN (Fig. 3F) was significantly greater in all groups relative to BL (C3, $p = 0.002$; D3, $p < 0.001$; C7, $p = 0.007$; D7, $p < 0.001$) and the concentration of PEN in D7 mice was significantly greater compared to C7 mice ($p = 0.029$) with a significant effect of diabetes ($p = 0.009$). The concentration of DPD (Fig. 3D) was significantly greater in D3 mice relative to BL ($p = 0.010$) and trended towards an increase in D7 mice relative to BL ($p = 0.073$). No differences between any groups or factor effects were detected for the divalent immature cross-links DHLNL (Fig. 3A) and HLNL (Fig. 3B). All groups exhibited significantly greater PYD relative to BL (Fig. 3C; C3, $p = 0.011$; D3, $p < 0.001$; C7, $p = 0.023$; D7, $p = 0.006$). No

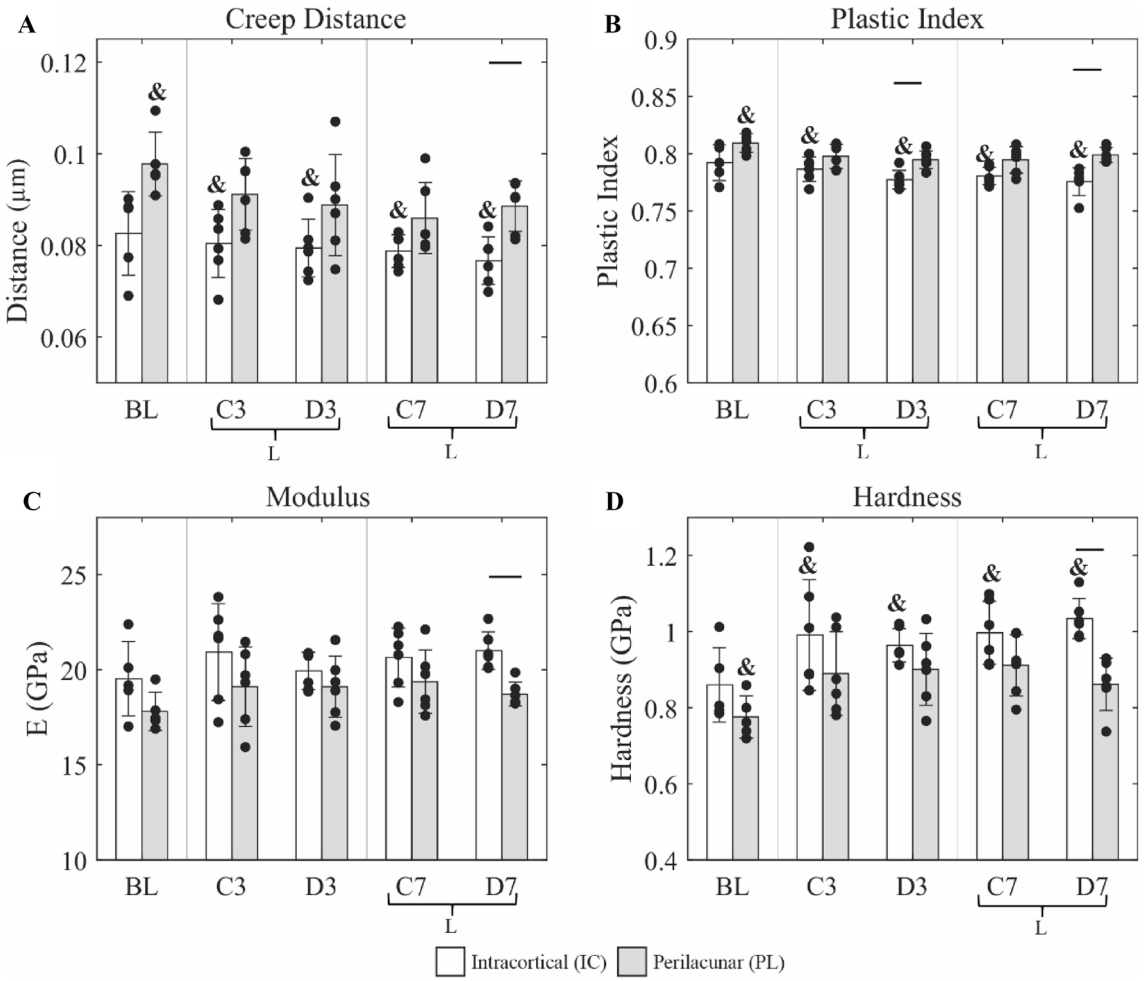

Fig. 4 Nanoindentation measures taken at intracortical (IC) and perilacunar (PL) regions. Local mechanical outcomes **A** creep distance, **B** plastic index, **C** modulus, **D** hardness for baseline (BL), 3-week control (C3), 3-week diabetic (D3), 7-week control (C7) and 7-week diabetic (D7) mice. Data is presented as mean ± standard deviation. Two-way ANOVAs were carried out for C3, D3 and separately for C7, D7 with control/diabetic and intracortical/lacunar as the two factors. Two-way ANOVAs were also carried out for BL compared to all groups, with group and location as the two factors. Differences relative to BL are noted by & ($p < 0.05$). Significant factor effects ($p < 0.05$) for diabetic status (D), location (L) and diabetic status-time interaction (DxL) are indicated below the x-axis. Trending differences ($0.05 < p < 0.10$) are noted with p-values above horizontal bars or above the italicized *&*

significant difference was detected in the concentration of pyrrolic crosslinks (Fig. 3E). No significant differences with diabetes were detected for any of the enzymatic collagen cross-link ratios, while PEN normalized to immature crosslinks, pyridinolines, and total number of enzymatic crosslinks yielded the same significant comparisons as PEN alone (Supp. Table 3).

7 weeks of Diabetes Decoupled Perilacunar and Intracortical Mechanical Properties and Increased Perilacunar 1660/1690 cm^{-1} Ratio

The nanoindentation procedure consisted of an applied load, then held at constant load to examine creep and viscoelastic behavior, followed by a period of unloading from which the traditional hardness and modulus values were obtained. Creep distance in D7 bones was significantly greater in the perilacunar zone relative to the intracortical region (Fig. 4 A, $p = 0.009$). Factor effects for location (L) were detected within the 3- and 7-week groups ($p = 0.008$, $p < 0.001$). Similarly, the plastic index which is the ratio of plastic work to total work, (Fig. 4B) in the perilacunar zone of D7 mice was significantly greater than in the intracortical tissue ($p = 0.003$). In D3 mice, the plastic index was significantly greater in perilacunar regions than intracortical ($p = 0.021$). The intracortical plastic index for all 3- and 7-week groups was also significantly lower than the baseline plastic index (C3IC, $p = 0.017$; D3IC, C7IC, D7IC, $p < 0.001$), with factor effects for location (L) within the 3- and 7-week groups ($p = 0.001$, $p < 0.001$). This collective data demonstrates that

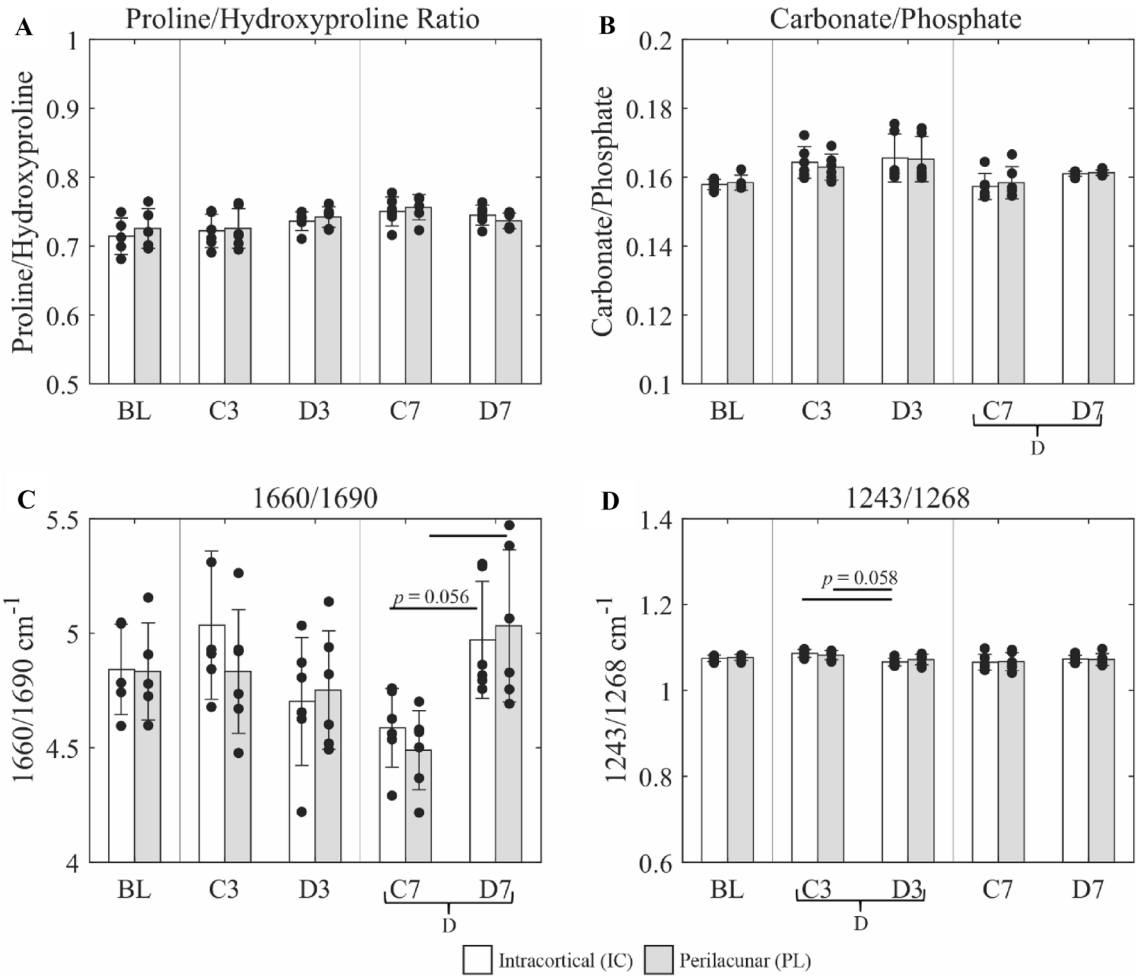

Fig. 5 Raman spectroscopy measures taken at intracortical (IC) and perilacunar (PL) regions. Measurements include **A** proline/hydroxyproline ratio, **B** carbonate/phosphate, **C** 1660 cm^{-1}/1690 cm^{-1}, and **D** 1243 cm^{-1}/1268 cm^{-1} for baseline (BL), 3-week control (C3), 3-week diabetic (D3), 7-week control (C7) and 7-week diabetic (D7) as mean ± standard deviation. Two-way ANOVAs were carried out for C3, D3 and separately for C7, D7 with control/diabetic and intracortical/lacunar as the two factors. Two-way ANOVAs were also carried out for BL compared to all groups with group and location as the two factors. Differences relative to BL are noted by & ($p < 0.05$). Significant factor effects ($p < 0.05$) for diabetic status (D), location (L) and diabetic status-time interaction (DxL) are indicated below the x-axis. Trending differences ($0.05 < p < 0.10$) are noted with p-values above horizontal bars or above the italicized *&*

the perilacunar region was more easily deformed under a constant load, with a greater creep distance relative to intracortical regions for the 7-week diabetic mice only. For the traditional nanoindentation measures, the modulus (Fig. 4C) in the perilacunar region of D7 mice was significantly lower compared to the intracortical region ($p = 0.026$) with a location factor effect for the 7-week timepoint ($p = 0.003$). The hardness (Fig. 4D) in the perilacunar zone was also significantly lower than in the intracortical region for D7 mice ($p = 0.002$). Factor effects for location (L) were detected within 7-week groups ($p < 0.001$). All nanoindentation outcomes are provided in Supplemental Table 4.

From the creep holding period, a viscoelastic Burgers model was fitted to the data. Significant differences between the perilacunar and intracortical tissue of D7 mice were detected for all Burgers model parameters: instantaneous modulus (E_1) and instantaneous viscosity (η_1) as well as the long-term modulus (E_2) and parallel viscosity (η_2), and plastic work. Collectively, the nanoindentation data demonstrates that D7 mice exhibited a decoupling of perilacunar and intracortical creep distance, modulus, hardness and Burgers model parameters, supporting a localized response to diabetes where the perilacunar zone is preferentially affected.

The amide I sub-band ratio (1660/1690 cm^{-1}, Fig. 5C) in the perilacunar zone of D7 mice was significantly greater compared to the perilacunar zone of C7 mice ($p = 0.004$). The matrix maturity in the intracortical region of D7 mice trended higher than the intracortical region of C7 mice ($p = 0.056$). A significant diabetes factor effect was

Table 1 Cortical bone morphology

	BL	C3	D3	C7	D7	Group effects
Cortical morphology—3D						
Total volume (Ct.TV, mm^3)	0.94 (0.08)	0.92 (0.29)	0.98 (0.08)	0.97 (0.06)	0.97 (0.08)	
Bone volume (Ct.BV, mm^3)	0.39 (0.03)	0.37 (0.11)	0.38 (0.02)	0.40 (0.02)	0.38 (0.03)	
Ct.BV/TV (%)	0.41 (0.01)	0.40 (0.02)	0.39$^{\&}$ (0.02)	0.41 (0.01)	0.39$^{\&}$ (0.02)	D
Ct.BMD (mg HA/cm^3)	501.2 (11.0)	492.7 (33.2)	488.1 (28.2)	509.7 (20.2)	481.6 (30.8)	
Ct.TMD (mg HA/cm^3)	1197.4 (7.9)	1222.6$^{\&}$ (22.7)	1226.1$^{\&}$ (17.2)	1237.3$^{\&}$ (17.3)	1231.6$^{\&}$ (20.1)	
Cortical morphology—2D						
Total area (Tt.Ar, mm^2)	1.97 (0.16)	2.10 (0.16)	2.04 (0.16)	2.03 (0.13)	2.03 (0.16)	
Cortical area (Ct.Ar, mm^2)	0.83 (0.06)	0.84 (0.05)	0.81 (0.05)	0.83 (0.04)	0.79 (0.07)	D
Marrow area (Ma.Ar, mm^2)	1.15 (0.11)	1.26$^{\&}$ (0.13)	1.23 (0.14)	1.20 (0.10)	1.24 (0.11)	
Thickness (Ct.Th, mm)	0.19 (0.01)	0.19 (0.01)	$0.18^{\&}$ (0.01)	0.19 (0.01)	$0.18^{\&}$ (0.01)	D
Perimeter (Ct.Pm, mm)	5.5 (0.2)	$5.7^{\&}$ (0.2)	5.6 (0.2)	5.6 (0.2)	5.6 (0.3)	
I_{ML}	0.14 (0.02)	0.15 (0.02)	0.14 (0.02)	0.14 (0.02)	0.14 (0.02)	
I_{AP}	0.30 (0.05)	0.34 (0.05)	0.31 (0.04)	0.32 (0.04)	0.30 (0.06)	

3D and 2D cortical morphology for baseline (BL), 3-week control (C3), 3-week diabetic (D3), 7-week control (C7) and 7 week diabetic (D7) mice. Data is presented as mean (standard deviation). Significant factor effects ($p < 0.05$) for diabetic status (D), time (T) and diabetic status-time interaction (DxT) are indicated in the right-most column. One-way ANOVAs with least-squares difference post-hoc tests were carried out to detect significant differences relative to BL and are indicated by & ($p < 0.05$)

Table 2 Pearson correlation coefficients between disease markers, whole-bone mechanical properties, morphology and local mechanical properties and composition

	Blood Glucose	HbA1c	Cortical BV/TV	Cortical BMD	Cortical Area	Stiffness	Ultimate Load	Post-Yield Work	Creep Distance (PL)	Creep Distance (IC)	Plastic Index (PL)	Plastic Index (IC)	1660/ 1690(PL)	1660/ 1690 (IC)	MMR (PL)	MMR (IC)
Blood Glucose		0.92	-0.42	-0.34	-0.31	-0.32	-0.40					-0.39				
HbA1c			-0.41	-0.32	-0.37	-0.37	-0.37					-0.37				
Cortical BV/TV				0.96		0.50										
Cortical BMD						0.48										
Cortical Area						0.32	0.52									
Stiffness							0.40									
Ultimate Load								0.31								
Post-Yield Work													-0.70	-0.46	0.46	0.53
Creep Distance (PL)										0.46	0.61					
Creep Distance (IC)												0.46				
Plastic Index (PL)												0.55				
Plastic Index (IC)																
1660/1690 (PL)														0.85		
1660/1690 (IC)																
MMR (PL)																0.91
MMR (IC)																

Only significant correlations ($p < 0.05$) are included in the table. Bone volume fraction (BV/TV), bone mineral density (BMD), intracortical (IC), perilacunar (PL), mineral-to-matrix ratio (MMR)

detected at 7-weeks as well ($p = 0.001$). The amide III ratio (1243/1268 cm^{-1}, Fig. 5D) was significantly lower at the intracortical region of D3 mice relative to C3 mice ($p = 0.012$) with a diabetic factor effect within the 3-week groups ($p = 0.001$). No significant difference was detected in the proline/hydroxyproline ratio between any groups

(Fig. 5A). A diabetic factor effect for the 7-week timepoint was detected for carbonate/phosphate ($p < 0.015$; Fig. 5B). No significant difference with diabetes was detected for mineral-to-matrix, or mineral crystallinity. All Raman spectroscopy measures are provided in the supplemental (Supp. Table 5).

There was no difference in osteocyte density (Supp. Figure 2B A), LOX + signal/area (Supp. Figure 2B) or RAGE + signal/area (Supp. Figure 2C) between any groups. These signal-based measurements were focused to a mask created from the DAPI signal to isolate osteocyte expression of LOX and RAGE. A diabetic factor effect was detected for RAGE + signal/area ($p = 0.029$).

Whole-Bone Morphology is Predictive of Whole-Bone Stiffness and Strength, While Local Tissue Composition is Predictive of Post-Yield Behavior

A correlation analysis was conducted to probe the relationships between whole-bone to whole-bone, local to local, and local to whole-bone measurements. Table 2 presents significant Pearson correlation coefficients across these length scales for key measures. Post-yield work was most strongly correlated with the 1660/1690 cm^{-1} ratio at the perilacunar ($R = -0.70$) and intracortical regions ($R = -0.46$) and the mineral-to-matrix measures at the perilacunar ($R = 0.46$) and intracortical regions ($R = 0.53$). Within local measurements, the plastic index and creep distance did not correlate with the 1660/1690 cm^{-1} ratio or the mineral-to-matrix levels. Generally, ultimate load and stiffness were better predicted by whole-bone measures of bone morphology, rather than by local properties. Whole-bone measures of Ct.BV/TV, Ct.BMD, and Ct.Ar strongly and significantly correlated with stiffness ($R = 0.50$, 0.48, 0.32, respectively), while only cortical area correlated with ultimate load ($R = 0.52$). These whole-bone measures did not correlate significantly with post-yield work. No nanoindentation measure correlated with whole-bone mechanical properties.

Ct.BV/TV explained 23% of the variance in stiffness (Fig. 6A) and cortical area explained 26% of the variance in ultimate load (Fig. 6B). Within the local measurements, the intracortical proline/hydroxyproline ratio explained 20% of the variance in intracortical plastic index (Fig. 6C) and the perilacunar 1660/1690 cm^{-1} ratio explained 14% of the variance in intracortical plastic work (Fig. 6D). Examining how local measurements correlate with whole-bone properties, the IC 1660/1690 cm^{-1} ratio explained only 17% of the post-yield work (Fig. 6E), while the perilacunar 1660/1690 cm^{-1} explained 46% of the variance (Fig. 6F). Meanwhile, intracortical mineral-to-matrix ratio explained 24% of the post-yield work (Fig. 6G), and the perilacunar mineral-to-matrix ratio explained 17% of the post-yield work (Fig. 6H).

Discussion

This is the first study to comprehensively characterize the local composition and mechanical properties of the perilacunar zone in bones from mice with diabetes and relate these local measures to whole-bone mechanical properties. Using an STZ model, hyperglycemia was induced in skeletally mature mice. After 3 weeks, mice exhibited significantly greater fasting blood glucose and HbA1c relative to controls, and these measures increased at 7 weeks, with a prevention of weight gain in both diabetic groups (Fig. 1).

Regarding the local tissue composition, the perilacunar zone in D7 mice exhibited significantly higher values in the 1660/1690 cm^{-1} Raman ratio compared to C7 mice, and trended greater in the intracortical region of D7 mice compared to C7 mice (Fig. 5C), with a diabetic factor effect for this ratio and carbonate-to-phosphate. There was no significant difference in mineral-to-matrix ratio, proline/hydroxyproline or mineral crystallinity between perilacunar and intracortical measures for any group (Supp. Table 5). The major impact of diabetes on local mechanical properties was an increased plastic index, and creep distance, and decreased modulus and hardness at the perilacunar zone relative to the intracortical tissue at 7 weeks (Fig. 4). While there were significant location effects at both 3 and 7-weeks for creep distance, and plastic index, the difference between perilacunar and intracortical tissue was most prominent in the diabetic group at 7 weeks, and absent in control groups at all timepoints. This decoupling of mechanical properties between perilacunar and intracortical regions indicates an increase in local mechanical heterogeneity with diabetes. Whether this increased gradient allows for more cracks to originate within the osteocyte lacunocanalicular network or is a compensatory mechanism against increased fragility remains unclear. Prior animal studies have found a reduction in hardness and modulus in STZ-treated mice [45], these reductions were modest and only evident after 15 weeks of diabetes [46]. The absence of differences in nanoindentation measures between the same location in diabetic vs. control animals (Fig. 4), but presence of IC-to-PL decoupling, suggests that this decoupling may occur earlier in the progression of the diabetic skeletal phenotype. However, while animal studies demonstrate a reduction in hardness and modulus, cadaveric studies are mixed with studies demonstrating an increased micro-hardness with T1D [47], and conflicting results with decreased [48], or increased [49] modulus and hardness with T2D.

The difference between PL and IC sites in creep distance, plastic index, and several of the Burgers model parameters (Supp. Table 4) with diabetes at the 7-week timepoint indicates a difference in the underlying collagen

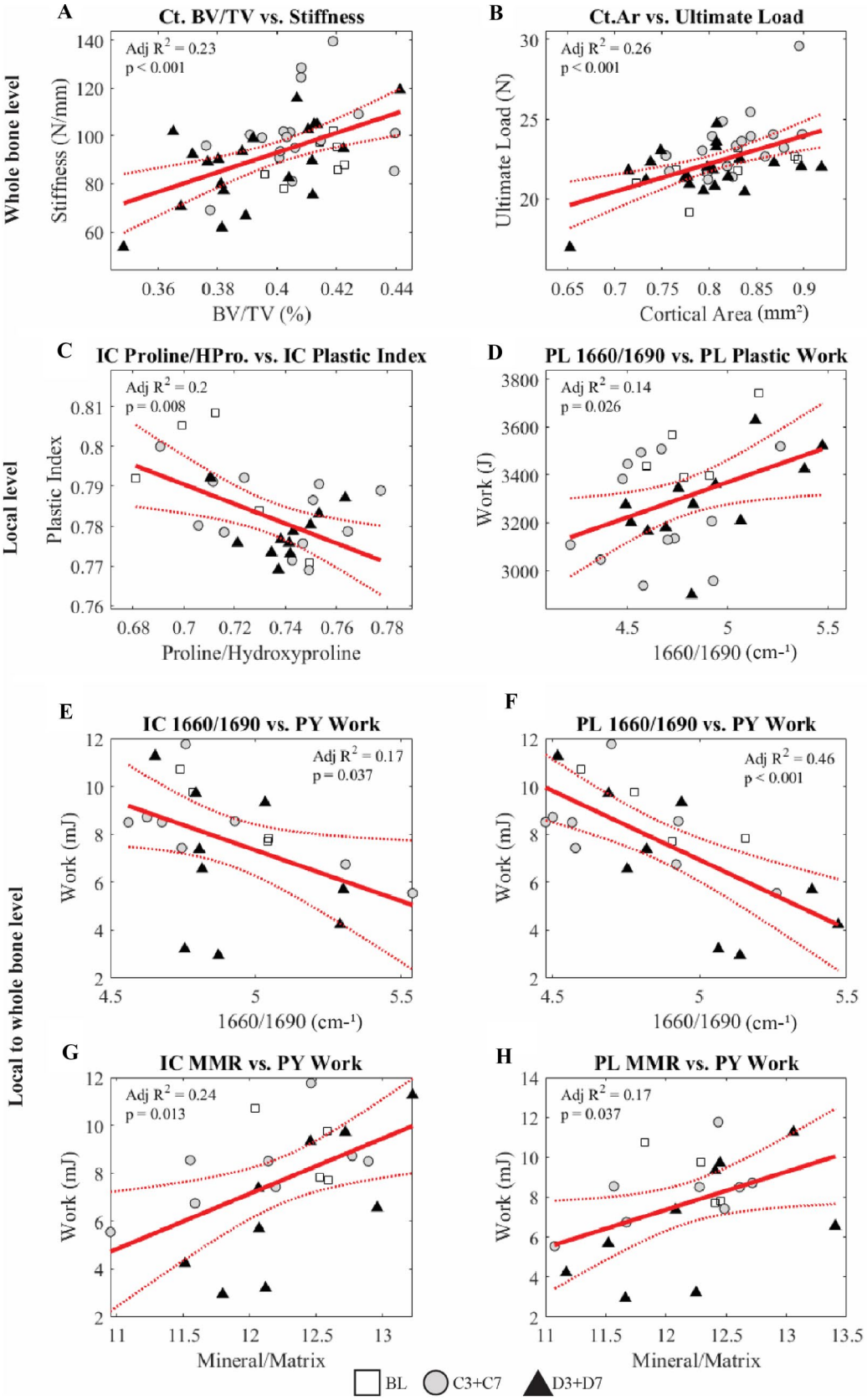
Whole bone level
Local level
Local to whole bone level
A
Ct. BV/TV vs. Stiffness
Adj R² = 0.23
p < 0.001
Stiffness (N/mm)
BV/TV (%)
B
Ct.Ar vs. Ultimate Load
Adj R² = 0.26
p < 0.001
Ultimate Load (N)
Cortical Area (mm²)
C
IC Proline/HPro. vs. IC Plastic Index
Adj R² = 0.2
p = 0.008
Plastic Index
Proline/Hydroxyproline
D
PL 1660/1690 vs. PL Plastic Work
Adj R² = 0.14
p = 0.026
Work (J)
1660/1690 (cm-1)
E
IC 1660/1690 vs. PY Work
Adj R² = 0.17
p = 0.037
Work (mJ)
1660/1690 (cm-1)
F
PL 1660/1690 vs. PY Work
Adj R² = 0.46
p < 0.001
Work (mJ)
1660/1690 (cm-1)
G
IC MMR vs. PY Work
Adj R² = 0.24
p = 0.013
Work (mJ)
Mineral/Matrix
H
PL MMR vs. PY Work
Adj R² = 0.17
p = 0.037
Work (mJ)
Mineral/Matrix
BL
C3+C7
D3+D7

◂**Fig. 6** Linear regressions between whole-bone measures **A** cortical bone volume fraction (Ct.BV/TV) vs. stiffness, **B** cortical area (Ct.Ar) vs. ultimate load; local to local relationships of **C** intracortical (IC) proline/hydroxyproline vs IC plastic index, and **D** perilacunar (PL) 1660 cm^{-1}/1690 cm^{-1} vs. post-yield (PY) work; and how local measurements relate to the whole-bone level **E** IC 1660 cm^{-1}/1690 cm^{-1} vs. PY work, **F** PL 1660 cm^{-1}/1690 cm^{-1} vs. PY work, **G** IC mineral-to-matrix ratio (MMR) vs. PY work, and **H** PL MMR vs. PY work. Linear fits are presented alongside 95% confidence intervals, with individual data points, and adjusted R^2 with p-value

matrix, which is thought to be more responsible for the viscoelastic response of bone. There is debate as to whether perilacunar remodeling is a resorption and redeposition of mineral and collagen, or just mineral [50]. Under diabetic conditions, osteocytes have increased sclerostin expression, with reduced viability and mechanosignaling [22], as well as altered osteocyte network organization [28]. These signaling and morphological changes suggest that osteocytes are less active, and may be less able to remodel their surrounding bone. The increased creep distance and plastic index at the perilacunar zone relative to intracortical tissue in the D7 group, but not C7, suggests that the perilacunar collagen matrix is more easily deformed in the diabetic state. This increased susceptibility of the collagen matrix to deformation may be due to a reduction in homeostatic perilacunar matrix remodeling, supported by the increase in the matrix maturity 1660/1690 ratio and supports the hypothesis that osteocytes are critical to maintaining not only the mineral but their surrounding collagen matrix.

For whole-bone morphology, there was no significant difference between diabetic groups and age-matched controls (Table 1). There were, however, significant diabetic factor effects for Ct.BV/TV, cortical area, and cortical thickness. The Ct.BV/TV and cortical thickness were also lower relative to BL, while the age-matched controls were not. Yet, the ultimate load and post-yield work were significantly lower in D7 mice relative to C7 mice, while in D7 relative to BL mice, post-yield displacement was significantly lower and stiffness and total work trended lower (Fig. 2). These differences are consistent with prior studies indicating a reduction in total load, and work-to-failure in high fat diet diabetic mice [25] and STZ-treated mice [29]. The lack of perturbation to whole-bone morphology in this model allowed us to explore the relative contribution of measures of bone quality, like local tissue composition to whole-bone mechanical behavior.

At the whole-bone level, the increase in PEN content in D7 mice, but not D3 mice (Fig. 3) highlights the important time-dependence of the disease state. The lack of difference in enzymatic collagen crosslinks, apart from an increase in deoxypyridinoline in D3 mice relative to BL was not surprising within the context of this study, given there was no significant difference in LOX + signal (Supp. Figure 2). The significant diabetic effect in RAGE + was intriguing given the increased PEN content (Supp. Figure 2), as an increase in PEN would be expected to occur contemporaneous to an increase in RAGE expression. No significant correlation existed between any directly measured collagen cross-link or PEN and LOX or RAGE signal (data not shown). As the majority of bone is deposited by 10–12 weeks of age, the effect of 3 or 7 weeks of diabetes on LOX, RAGE, and enzymatic cross-links, may be less pronounced compared to states of more rapid bone growth under diabetic conditions, as LOX is prevalent at sites of bone formation. Animal ages were chosen to minimize the confounding effect of diabetes on bone growth, as STZ-induced diabetes impairs bone length in growing rats [51], and to better isolate the role of local tissue in the progression of STZ-induced diabetic fragility. Additionally, as we were focused on the progression and development of the diabetic skeletal phenotype, we chose to limit the duration of diabetes to 7 weeks, where an increased duration of diabetes in mature animals would likely have greater AGE accumulation.

After detecting diabetes-related differences at the local perilacunar and whole-bone levels, the second aim of this study was to understand the relative importance of local perilacunar mechanical properties and composition to whole-bone mechanical properties. Mechanical properties of particular interest were ultimate load and post-yield work, as these properties were most affected by diabetes (Fig. 2). Geometrical measures like Ct.BV/TV did explain 23% of the variance in stiffness, and cortical area explained 26% of the variance in ultimate load (Fig. 6). However, none of these whole-bone geometrical measures predicted post-yield work (Table 2). The strongest predictor of post-yield work was local composition. The perilacunar 1660/1690 cm^{-1} ratio explained 46% of the variance in post-yield work, seeing a decrease in post-yield work with increasing 1660/1690 cm^{-1} ratio values, while the intracortical 1660/1690 cm^{-1} ratio explained only 17% of the post-yield work (Fig. 6). The greater explanatory power of the perilacunar zone highlights the relative importance of the collagen matrix at the perilacunar region relative to the intracortical regions measured to whole-bone mechanical properties. The importance of the perilacuanar zone should not be interpreted as a direct causality link between perilacunar composition and whole-bone post-yield behavior, but rather an emphasis on the importance of the perilacunar zone relative to intracortical regions. Many studies incorporating spectroscopic and nanoindentation [45–47] measures explicitly avoid indenting near lacunae. An alternative approach including perilacunar regions may allow assessment of osteocyte function and maintenance of tissue surrounding the osteocyte, as well as the mechanical contribution of the perilacunar regions to whole-bone behavior. The mineral-to-matrix ratio at the intracortical and perilacunar locations explained 24%

and 17% of the post-yield work, respectively. Nanoindentation measures did not correlate significantly with either whole-bone or estimated tissue-level mechanical properties (Table 2). Summarizing the relationships between whole-bone mechanics and measured properties, ultimate load was best predicted by whole-bone geometry, while post-yield work was most predicted by local composition. The importance of whole-bone geometry suggests that an imbalance in bone formation/resorption of the tissue relative to healthy controls is contributing to the strength decline, but tissue-level properties and composition are more impactful for decreased brittleness with diabetes.

Local mechanical properties measured via nanoindentation only weakly correlated with local composition measured via Raman. The perilacunar 1660/1690 cm^{-1} ratio was able to explain only 14% of the variance in nanoindentation plastic work (Fig. 6), suggesting there are other factors besides those measured with Raman spectroscopy contributing to this divergence of mechanical properties between the intracortical and perilacunar regions. The significant regional differences in mechanical behavior between intracortical and perilacunar tissue, absent location differences in Raman measures suggests that this mechanical gradient is not fully dependent on composition, at least as measured by Raman spectroscopy. Other factors dictating local mechanical properties, could be the osteocyte canalicular network which is perturbed in a diabetic state—including a increased canalicular node degree [28], or parameters of matrix organization that are not directly measured by Raman spectroscopy such as tissue glycation, or non-collagenous proteins. Additionally, that the perilacunar 1660/1690 cm^{-1} ratio is more predictive of whole-bone post-yield work than local plastic work supports that the nanoindentation outcomes are not dependent on the local Raman spectroscopy measures. This counterintuitive relationship between local nanoindentation and composition is contradictory to work which showed strong predictive power of mineral-to-matrix ratio for hardness and plastic index [43, 52]. However, these studies examined healthy bone tissue, the methodology in these studies allowed for Raman measurements and indents to be taken at the same location, and there was a wider range of measured values.

The physiological meaning of the 1660/1690 cm^{-1} Raman ratio is not definitively established. Several groups have presented the 1660/1690 cm^{-1} ratio as a measure of mature/immature cross-links [53, 54], while others have found that this ratio is not specific to direct measurements of this enzymatic cross-link ratio [55]. The lack of any significant difference in the ratio of cross-link maturity, mature or immature cross-links with diabetes (Fig. 3, Supp. Table 3) as measured by HPLC, but a difference in the 1660/1690 cm^{-1} Raman ratio in both perilacunar and intracortical sites supports that this ratio is related to collagen secondary structure [55], or is a measure of collagen or "matrix maturity" rather than specific cross-link ratios [37, 56, 57]. The increase in the 1660/1690 cm^{-1} ratio (Fig. 5) also occurred contemporaneous to an increase in pentosidine (Fig. 3). Due to experimental constraints, these measurements were not taken on the same animal or bone, so correlations to direct measurements of collagen cross-links or pentosidine were not possible. Nonetheless, increases in the 1660/1690 cm^{-1} ratio occur with age [53], lysyl oxidase inhibition [37], and in a different diabetic mouse model [21]. This more conservative attribution of "matrix maturity" to the 1660/1690 cm^{-1} ratio was chosen for this study.

This study focused on measuring the effects of diabetes on the properties of the perilacunar zone, using intracortical measures as relative controls. It is likely that diabetes and hyperglycemic conditions also affect areas of newly formed tissue like the periosteal and endosteal surfaces and future work should seek to understand the relative importance of perilacunar composition in the context of those newly formed regions of bone. There are sub-micron level differences in mechanical properties in the perilacunar matrix and the gradient is steeper near osteocytes in newly formed tissue compared to tissue surrounding intracortical osteocytes [58]. Sub-micron resolution was not possible with the nanoindentation system used in this study, and examination of this gradient at a finer scale may better elucidate the decoupling of local mechanical properties between intracortical and perilacunar sites with diabetes. The Raman and nanoindentation measurements were taken on transverse sections, and it is possible that some intracortical measurements were not greater than 20 µm away from lacunae below the polished surface. Additionally, due to tissue allocation constraints, direct cross-link measures were not able to be correlated against whole-bone mechanical properties or local composition and mechanical measurements.

The choice of diabetic animal model should also be carefully considered when extrapolating these findings to the presentation of type 1 or type 2 diabetes in humans. One of the limitations of the STZ model is that it is a chemical administered to kill the insulin producing β cells, not an autoimmune elimination of β cells as seen clinically with type 1 diabetes. This study focused on the progression and development of diabetic skeletal fragility with respect to the perilacunar tissue. The advantage of the STZ diabetes model is greater control of disease induction, replicability, and longevity of animals after disease confirmation with only a slight reduction in weight. Other models mimicking T1D have a more unpredictable disease induction. Mouse models of T2D add the confounding variable of body weight to the interpretation of the diabetic skeletal phenotype. Thus, the STZ model was chosen as the model to examine the effect of hyperglycemia on an adolescent-to-adult aged bone over a 7-week period, and without large differences in mouse weight. How the perilacunar tissue

and osteocyte network differ in a type 2 model of diabetes, where osteoblasts and osteocytes may develop insulin resistance is an area for future exploration.

This work highlights the importance of the perilacunar zone compared to intracortical regions to whole-bone mechanical properties in diabetes and, more generally, with age or other disease states. Whether perilacunar composition and mechanical properties can be recovered to healthy levels with lifestyle (e.g. exercise) or pharmacologic intervention (e.g. PTH) should be evaluated for diabetes and other conditions where the perilacunar tissue and remodeling are perturbed. This work provides a better understanding of the mechanisms of diabetic skeletal fragility and opens avenues for the design of therapies to target these local regions within the bone that are most negatively affected.

Conclusions

The major conclusions and novelty of this study are two-fold. This is the first demonstration that STZ-induced diabetes increases matrix maturity at both intracortical and perilacunar regions, and that STZ-induced diabetes also caused a decoupling between intracortical and perilacunar mechanical properties. Both changes were only evident in mice having diabetes for 7 weeks, highlighting the time-dependent nature of the effect of diabetes on bone composition. Secondly, this is the first study to reveal a contribution of perilacunar tissue composition to whole-bone mechanical properties in diabetics—i.e. the contribution of perilacunar "matrix maturity" to post-yield work. Perilacunar "matrix maturity" was more predictive of post-yield work than intracortical measures or any whole-bone morphological measures, highlighting the importance of the perilacunar tissue to whole-bone mechanical properties.

Supplementary Information The online version contains supplementary material available at https://doi.org/10.1007/s00223-023-01098-9.

Acknowledgements We would like to thank Gurjit Mandair for training and assistance with Raman spectroscopy, and Ken Kozloff for use of the nanoindentation system. This work was supported by was supported by T32 DE007057, and P30AR069620. The content of this work is solely the responsibility of the authors and does not necessarily represent the official views of the National Institutes of Health.

Declarations

Conflict of interest The authors (MB, TT, DK) have no financial or non-financial interests to disclose that are related to this publication.

Human and Animal Rights All animal procedures and protocols were conducted with approval from the University of Michigan Institutional Animal Care and Use Committee (IACUC).

Informed Consent This article does not contain any studies with human subjects performed by any of the authors. For this type of study, formal consent is not required.

References

1. Vestergaard P (2007) Discrepancies in bone mineral density and fracture risk in patients with type 1 and type 2 diabetes–a meta-analysis. Osteoporos Int 18(4):427–444. https://doi.org/10.1007/s00198-006-0253-4
2. Merlotti D, Gennari L, Dotta F, Lauro D, Nuti R (2010) Mechanisms of impaired bone strength in type 1 and 2 diabetes. Nutr Metab Cardiovasc Dis 20(9):683–690. https://doi.org/10.1016/j.numecd.2010.07.008
3. Napoli N et al (2017) Mechanisms of diabetes mellitus-induced bone fragility. Nat Rev Endocrinol 13(4):208–219. https://doi.org/10.1038/nrendo.2016.153
4. Leanza G et al (2019) Risk factors for fragility fractures in type 1 diabetes. Bone 125:194–199. https://doi.org/10.1016/j.bone.2019.04.017
5. Saito M, Marumo K (2010) Collagen cross-links as a determinant of bone quality: a possible explanation for bone fragility in aging, osteoporosis, and diabetes mellitus. Osteoporos Int 21(2):195–214. https://doi.org/10.1007/s00198-009-1066-z
6. Acevedo C et al (2018) Contributions of material properties and structure to increased bone fragility for a given bone mass in the UCD-T2DM rat model of type 2 diabetes. J Bone Miner Res 33(6):1066–1075. https://doi.org/10.1002/jbmr.3393
7. Garnero P (2012) The contribution of collagen crosslinks to bone strength. Bonekey Rep 1:182. https://doi.org/10.1038/bonekey.2012.182
8. Siegmund T, Allen MR, Burr DB (2008) Failure of mineralized collagen fibrils: Modeling the role of collagen cross-linking. J Biomech 41(7):1427–1435. https://doi.org/10.1016/j.jbiomech.2008.02.017
9. Bonewald LF (2011) The amazing osteocyte. J Bone Miner Res 26(2):229–238. https://doi.org/10.1002/jbmr.320
10. Vahidi G, Rux C, Sherk VD, Heveran CM (2021) Lacunar-canalicular bone remodeling: Impacts on bone quality and tools for assessment. Bone 143:115663. https://doi.org/10.1016/j.bone.2020.115663
11. Buenzli PR, Sims NA (2015) Quantifying the osteocyte network in the human skeleton. Bone 75:144–150. https://doi.org/10.1016/j.bone.2015.02.016
12. Qing H et al (2012) Demonstration of osteocytic perilacunar/canalicular remodeling in mice during lactation. J Bone Miner Res 27(5):1018–1029. https://doi.org/10.1002/jbmr.1567
13. McNerny EMB, Gardinier JD, Kohn DH (2015) Exercise increases pyridinoline cross-linking and counters the mechanical effects of concurrent lathyrogenic treatment. Bone 81:327–337. https://doi.org/10.1016/j.bone.2015.07.030
14. Gardinier JD, Al-Omaishi S, Morris MD, Kohn DH (2016) PTH signaling mediates perilacunar remodeling during exercise. Matrix Biol 52–54:162–175. https://doi.org/10.1016/j.matbio.2016.02.010
15. Taylor EA et al (2020) Sequential treatment of estrogen deficient, osteopenic rats with alendronate, parathyroid hormone (1–34), or raloxifene alters cortical bone mineral and matrix composition. Calcif Tissue Int 106(3):303–314. https://doi.org/10.1007/s00223-019-00634-w
16. Lane NE et al (2006) Glucocorticoid-treated mice have localized changes in trabecular bone material properties and osteocyte lacunar size that are not observed in placebo-treated or estrogen-deficient mice. J Bone Miner Res 21(3):466–476. https://doi.org/10.1359/JBMR.051103
17. Dole NS et al (2017) Osteocyte-intrinsic TGF-β signaling regulates bone quality through perilacunar/canalicular remodeling. Cell Rep 21(9):2585–2596. https://doi.org/10.1016/j.celrep.2017.10.115

18. Tang SY, Herber R-P, Ho SP, Alliston T (2012) Matrix metalloproteinase–13 is required for osteocytic perilacunar remodeling and maintains bone fracture resistance. J Bone Miner Res 27(9):1936–1950. https://doi.org/10.1002/jbmr.1646
19. Damrath JG, Moe SM, Wallace JM (2022) Calcimimetics alter periosteal and perilacunar bone matrix composition and material properties in early chronic kidney disease. J Bone Miner Res 37(7):1297–1306. https://doi.org/10.1002/jbmr.4574
20. Rolvien T et al (2017) Vitamin D regulates osteocyte survival and perilacunar remodeling in human and murine bone. Bone 103:78–87. https://doi.org/10.1016/j.bone.2017.06.022
21. Rubin MR et al (2016) Advanced glycation endproducts and bone material properties in type 1 diabetic mice. PLoS ONE 11:e0154700. https://doi.org/10.1371/journal.pone.0154700
22. Kalaitzoglou E, Popescu I, Bunn RC, Fowlkes JL, Thrailkill KM (2016) Effects of type 1 diabetes on osteoblasts, osteocytes, and osteoclasts. Curr Osteoporos Rep 14(6):310–319. https://doi.org/10.1007/s11914-016-0329-9
23. Gortázar AR, Ardura JA (2020) Osteocytes and diabetes: altered function of diabetic osteocytes. Curr Osteoporos Rep 18(6):796–802. https://doi.org/10.1007/s11914-020-00641-z
24. Parajuli A et al (2015) Bone's responses to mechanical loading are impaired in type 1 diabetes. Bone 81:152–160. https://doi.org/10.1016/j.bone.2015.07.012
25. García-Martín A et al (2012) Circulating levels of sclerostin are increased in patients with type 2 diabetes mellitus. J Clin Endocrinol Metab 97(1):234–241. https://doi.org/10.1210/jc.2011-2186
26. Notsu M et al (2017) Advanced glycation end product 3 (AGE3) increases apoptosis and the expression of sclerostin by stimulating TGF-β expression and secretion in osteocyte-like MLO-Y4-A2 cells. Calcif Tissue Int 100(4):402–411. https://doi.org/10.1007/s00223-017-0243-x
27. Piccoli A et al (2020) Sclerostin regulation, microarchitecture, and advanced glycation end-products in the bone of elderly women with type 2 diabetes. J Bone Miner Res 35(12):2415–2422. https://doi.org/10.1002/jbmr.4153
28. Mabilleau G, Perrot R, Flatt PR, Irwin N, Chappard D (2016) High fat-fed diabetic mice present with profound alterations of the osteocyte network. Bone 90:99–106. https://doi.org/10.1016/j.bone.2016.06.008
29. Maycas M et al (2017) PTHrP-derived peptides restore bone mass and strength in diabetic mice: additive effect of mechanical loading. J Bone Miner Res 32(3):486–497. https://doi.org/10.1002/jbmr.3007
30. Gustafson MB et al (1996) Calcium buffering is required to maintain bone stiffness in saline solution. J Biomech 29(9):1191–1194. https://doi.org/10.1016/0021-9290(96)00020-6
31. Gardinier JD, Mohamed F, Kohn DH (2015) PTH signaling during exercise contributes to bone adaptation. J Bone Miner Res 30(6):1053–1063. https://doi.org/10.1002/jbmr.2432
32. Schneider CA, Rasband WS, Eliceiri KW (2012) NIH Image to ImageJ: 25 years of image analysis. Nat Methods. https://doi.org/10.1038/nmeth.2089
33. Bouxsein ML, Boyd SK, Christiansen BA, Guldberg RE, Jepsen KJ, Müller R (2010) Guidelines for assessment of bone microstructure in rodents using micro–computed tomography. J Bone Miner Res 25(7):1468–1486. https://doi.org/10.1002/jbmr.141
34. Wallace JM, Golcuk K, Morris MD, Kohn DH (2009) Inbred strain-specific response to biglycan deficiency in the cortical bone of C57BL6/129 and C3H/He mice. J Bone Miner Res 24(6):1002–1012. https://doi.org/10.1359/jbmr.081259
35. Currey JD (1979) Mechanical properties of bone tissues with greatly differing functions. J Biomech 12(4):313–319. https://doi.org/10.1016/0021-9290(79)90073-3
36. Ritchie RO, Koester KJ, Ionova S, Yao W, Lane NE, Ager JW (2008) Measurement of the toughness of bone: a tutorial with special reference to small animal studies. Bone 43(5):798–812. https://doi.org/10.1016/j.bone.2008.04.027
37. McNerny EMB, Gong B, Morris MD, Kohn DH (2015) Bone fracture toughness and strength correlate with collagen cross-link maturity in a dose-controlled lathyrism mouse model. J Bone Miner Res 30(3):455–464. https://doi.org/10.1002/jbmr.2356
38. Bolger MW et al (2020) External bone size identifies different strength-decline trajectories for the male human femora. J Struct Biol 212:107650. https://doi.org/10.1016/j.jsb.2020.107650
39. Roberts HC, Knott L, Avery NC, Cox TM, Evans MJ, Hayman AR (2007) Altered collagen in tartrate-resistant acid phosphatase (TRAP)-deficient mice: a role for TRAP in bone collagen metabolism. Calcif Tissue Int 80(6):400–410. https://doi.org/10.1007/s00223-007-9032-2
40. Brown S, Worsfold M, Sharp C (2001) Microplate assay for the measurement of hydroxyproline in acid-hydrolyzed tissue samples. Biotechniques 30:38–40. https://doi.org/10.2144/01301bm06
41. Wu Z, Baker TA, Ovaert TC, Niebur GL (2011) The effect of holding time on nanoindentation measurements of creep in bone. J Biomech 44(6):1066–1072. https://doi.org/10.1016/j.jbiomech.2011.01.039
42. Oliver WC, Pharr GM (1992) An improved technique for determining hardness and elastic modulus using load and displacement sensing indentation experiments. J Mater Res 7(6):1564–1583. https://doi.org/10.1557/JMR.1992.1564
43. Raghavan M, Sahar ND, Kohn DH, Morris MD (2012) Age-specific profiles of tissue-level composition and mechanical properties in murine cortical bone. Bone 50(4):942–953. https://doi.org/10.1016/j.bone.2011.12.026
44. Mandair GS, Oest ME, Mann KA, Morris MD, Damron TA, Kohn DH (2020) Radiation-induced changes to bone composition extend beyond periosteal bone. Bone Rep 12:100262. https://doi.org/10.1016/j.bonr.2020.100262
45. Mansur SA et al (2015) Stable incretin mimetics counter rapid deterioration of bone quality in type 1 diabetes mellitus. J Cell Physiol 230(12):3009–3018. https://doi.org/10.1002/jcp.25033
46. Nyman JS et al (2011) Increasing duration of type 1 diabetes perturbs the strength–structure relationship and increases brittleness of bone. Bone 48(4):733–740. https://doi.org/10.1016/j.bone.2010.12.016
47. Farlay D, Armas LA, Gineyts E, Akhter MP, Recker RR, Boivin G (2016) Nonenzymatic glycation and degree of mineralization are higher in bone from fractured patients with type 1 diabetes mellitus. J Bone Miner Res 31(1):190–195. https://doi.org/10.1002/jbmr.2607
48. Sihota P et al (2021) Investigation of mechanical, material and compositional determinants of human trabecular bone quality in type 2 diabetes. J Clin Endocr Metab. https://doi.org/10.1210/clinem/dgab027
49. Lekkala S, Sacher SE, Taylor EA, Williams RM, Moseley KF, Donnelly E (2023) Increased advanced glycation endproducts, stiffness, and hardness in iliac crest bone from postmenopausal women with type 2 diabetes mellitus on insulin. J Bone Miner Res 38(2):261–277. https://doi.org/10.1002/jbmr.4757
50. Yee CS, Schurman CA, White CR, Alliston T (2019) Investigating osteocytic perilacunar/canalicular remodeling. Curr Osteoporos Rep 17(4):157–168. https://doi.org/10.1007/s11914-019-00514-0
51. Silva MJ et al (2009) Type 1 diabetes in young rats leads to progressive trabecular bone loss, cessation of cortical bone growth, and diminished whole bone strength and fatigue life. J Bone Mineral Res 24:1618–1627. https://doi.org/10.1359/jbmr.090316
52. Donnelly E, Boskey AL, Baker SP, van der Meulen MCH (2010) Effects of tissue age on bone tissue material composition and

nanomechanical properties in the rat cortex. J Biomed Mater Res Part A 92A(3):1048–1056. https://doi.org/10.1002/jbm.a.32442
53. Paschalis EP, Verdelis K, Doty SB, Boskey AL, Mendelsohn R, Yamauchi M (2001) Spectroscopic characterization of collagen cross-links in bone. J Bone Miner Res 16(10):1821–1828. https://doi.org/10.1359/jbmr.2001.16.10.1821
54. Takahata M et al (2012) Mechanisms of bone fragility in a mouse model of glucocorticoid-treated rheumatoid arthritis: implications for insufficiency fracture risk. Arthritis Rheum 64(11):3649–3659. https://doi.org/10.1002/art.34639
55. Farlay D et al (2011) The ratio 1660/1690 cm(-1) measured by infrared microspectroscopy is not specific of enzymatic collagen cross-links in bone tissue. PLoS ONE 6:e28736. https://doi.org/10.1371/journal.pone.0028736
56. Mandair GS, Morris MD (2015) Contributions of Raman spectroscopy to the understanding of bone strength. Bonekey Rep 4:620. https://doi.org/10.1038/bonekey.2014.115
57. Unal M et al (2018) Assessing glycation-mediated changes in human cortical bone with Raman spectroscopy. J Biophoton 11:e201700352. https://doi.org/10.1002/jbio.201700352
58. Rux CJ, Vahidi G, Darabi A, Cox LM, Heveran CM (2022) Perilacunar bone tissue exhibits sub-micrometer modulus gradation which depends on the recency of osteocyte bone formation in both young adult and early-old-age female C57Bl/6 mice. Bone 157:116327. https://doi.org/10.1016/j.bone.2022.116327